CENTRO DE INVESTIGACIONES EN ÓPTICA, A.C.

“Second Harmonic Generation as an optical probe of buried interfaces”

MAESTRÍA EN CIENCIAS (ÓPTICA)

Asesor(es): Dr. Bernardo Mendoza Santoyo

Estudiante: Sergio Felipe Beltrán Valencia

Agosto 2019
León, Guanajuato, México

Second Harmonic Generation as an optical probe of buried interfaces

by

Sergio Felipe Beltrán Valencia

A thesis submitted in partial fulfillment of the requirements
for the degree of Master of Science.

Advisor:
Dr. Bernardo Mendoza Santoyo

Centro de Investigaciones en Óptica, A.C.
Loma del Bosque 115, León, Guanajuato, 37150, México

August 27, 2019

The research presented in this thesis was carried out at the Centro de Investigaciones en Óptica, A.C., Loma del Bosque 115, León de los Aldama, Guanajuato, 37150, Mexico. Funding was provided by the CONACYT-México (Consejo Nacional de Ciencia y Tecnología), through scholarship No 491445.

SECOND HARMONIC GENERATION AS AN OPTICAL PROBE OF BURIED INTERFACES

by

Sergio Felipe Beltrán Valencia

Approved:

Dr. Bernardo Mendoza Santoyo
Thesis Advisor

Dr. Ramón Carriles Jaimes
Reader

Dr. Roberto Ramírez Alarcón
Reader

Centro de Investigaciones en Óptica, A.C.
Loma del Bosque 115, León, Guanajuato, 37150, México
August 27, 2019

"It is difficult to understand the universe if you only study one planet."

Miyamoto Musashi

Abstract

In this manuscript, we present a method for the determination of defects in the crystalline morphology of buried surfaces using SHG. This is done by calculating the second order nonlinear susceptibility using DFT, length gauge and the cut function for surface responses. We analyzed the change in the SHG response of GaAs 110 crystalline slabs due to systematically induced defects. We found that SHG can be used to obtain the position of periodical defects like the displacement of a atom in the periodic crystalline cell, also, SHG can be used to detect dislocation of sections in the slab and misfits between stacked slabs. Finally, we give a scheme for the experimental determination of this defects by using the values of nonlinear susceptibility measurements.

Acknowledgements

This thesis is the culmination of two years of work. I am very grateful to the people that helped me along the way. First I want to thank to my thesis advisor Bernardo Mendoza for guiding me in the development of this work and for all the corrections of this poorly written manuscript. I am very grateful with professor Geminiano for his teachings and for give me the opportunity to work with him. I want to thank my friends from the propedeutic course: Daniel, Nata, Yanier, Danay and Azael for explaining me several times the triangle problem and all the beans I have eat along this two years.

I want to thank my friends from the regular classes Juanjo, Cristian, Tarek and Mariana, among others, for all the good and funny moments; also Cristian and Tarek need a special mention for helping me along the dark moments in the calculations.

I also wish to thank my family in Colombia, nothing of this would have been possible without their support and comprehension.

Finally I want to thank Karen for her help in all aspects of my life, also because I would not have been able to start this master degree nor find the PhD of my dreams without her help.

Contents

List of Figures

List of Tables

1 Introduction

Outline

Ferroelectric materials are essential components in a wide spectrum of applications like RF devices, tunable microwave circuits and nonvolatile memories like Solid State Drives [1]. With the development of deposition techniques for thin films a new range of applications has arise due to size minimization and several kinds of nonlinear effects. However with the minimization of the size of this components, new problems have arisen, specially in interfaces between substrates and different deposited materials, like the integration of ferroelectrics with silicon for optoelectronic devices [2]. These films composed of slabs of different materials are known as buried surfaces. This interfaces usually present atom scale defects that can alter the nonlinear optical response of this materials. To overcome the challenges in the fabrication of buried surfaces, an analysis of the interface defects like displacements and mismatched interfaces has to be made. For this, Second Harmonic Generation (SHG) is a suitable candidate because of its properties, as it will be expained in this thesis.

SHG has been widely used to characterize several kinds of materials as it is a non-invasive technique, has high sensibility to symmetry changes and its good cost-efficiency relation. Some applications include the study of solid-solid, vacuum-solid and liquid-liquid interfaces [3–6]. Moreover, it can also be used for measuring defects in surfaces of both centrosymmetric and non-centrosymmetric media [7–9]. In recent years, there has been investigation towards the development of SHG tomography in vivo via fluorescence and optical coherence tomography [10–12]. On the other hand, even though the macroscopical description of non-linear optics is well developed [13], SHG and surface SHG calculations can be limited due to the lack of our understanding of low scale systems and interactions that generate non-linear responses; therefore, there is an inability to obtain accurate and experimentally-consistent calculations. In order to improve this weak points, several research have been done to improve the SHG range of action from first principles calculations [14–17]. A common source of error is the inability to efficiently calculate the gap for semi-conductors, this can be fixed by including a scissors operator that moves conduction bands rigidly to get a separation in agreement with experiment or with a previous GW calculation [18–20], providing an improvement over the calculation of linear optical responses; also the value for gap can be fully calculated with a full GW calculation, which introduces corrections over the full symmetry path and to the wave

functions energies, yet this can be more expensive than another kind of improvements. The optical responses can be enhanced by including the non-local part of the pseudo-potentials used for the DFT-LDA calculations [21–23]. Another point for improvement is the introduction of the Many Body contribution; this is necessary to calculate well the second order susceptibility regarding its non-linear properties; specifically the "length gauge" and its equivalent, the "velocity gauge", both correct the scissors operator for the calculation of the second order non-linear susceptibility [24, 25]. In the same way, several works accomplished advances in including bulk, intra-band and inter-band transitions, 1ω and 2ω resonance effects [26, 27]. In addition, to be able to extend SHG calculations to effectively simulate surface effects from first principles and correctly analyze the symmetry breaking effects considering interfaces and surface misfits, the cut function was introduced in Ref. [28]. This function might be used to extract the contribution of given parts of the crystalline super-cell. Recent works include the calculation of SHG in nano composites [29], an analysis of the effect of the nonresonant approximation commonly used in abinitio calculations for SHG [30], the inclusion of nonlocal operators for the SHG calculation [31], second-harmonic microscopy of strain fields around through-silicon-vias [32], the direct implementation of nonlocal operators and the cut function for semiconductor surfaces [33] and the implementation of the three layer model for calculation of the SHG response in surfaces at the border of bulk materials [34–36].

Even though ferroelectric materials have a natural SHG signal due the noncentrosymmetry of its crystalline structure, their efficient calculation is still theoretically and numerically challenging and under debate, yet a test model with another material can be used to prove if SHG is sensible to the defects that the deposition of films of ferroelectric materials have presented.

Finally, the objective of this work is to prove that SHG can be used to detect crystalline defects in buried surfaces of noncentrosymmetric materials, this can be done by implementing a structured library of crystalline defects that can be used to compare with the SHG response of experimental measurements.

This thesis is divided as follows: There is a review of some concepts that will be useful to explain the methodology in chapter 2. In chapter 3 we will describe the method for the study of the system and its defects. Results and their analysis will be presented in chapter 4. Finally, in chapter 5 are the final remarks and conclusions of the work.

2 Theoretical Framework

Outline

2.1 Cut function formalism

In order to analyze the optical properties of buried surfaces, it is convenient to introduce a method to calculate the contribution of the different sections of the material to these optical properties. We can think of a buried material as a superposition of layers of the same material, which are misaligned or have periodical defects due to the different process that can arise during the deposition of the material. This buried material will be represented as a slab, this is a crystalline surface with a finite size in z direction, and an infinite size in the x and y directions This is shown in figure 2.1, each layer will contain all the atoms of the slab inside a δz interval. The construction of this infinite slab is done by using the Bloch Theorem and working in the reciprocal space. A reciprocal space is a periodic set of points in this space, and contains the points that compose the Fourier transform of a periodic spatial lattice. So the cell in the figure 2.1 will be repeated in the three Cartesian coordinates. Also, if the vacuum space included in the z direction is large enough, there will not be interactions between atoms in different slabs, so the interactions and optical responses will correspond to the ones of a single layer [37].

A convenient way to calculate the contribution to the optical properties of different sections of the crystalline slab of a given material is to introduce a "cut function", $\mathcal{C}(z)$, which is usually taken to be unity over one half of the slab and zero over the other half [31, 38]. In this case $\mathcal{C}(z)$ will give the contribution of the side of the slab for which $\mathcal{C}(z) = 1$. As was done for the linear optical response [37], we can generalize this simple choice for $\mathcal{C}(z)$ by a top-hat cut function $\mathcal{C}^{\ell}(z)$ that selects a given layer,

$$\mathcal{C}^{\ell}(z) = \Theta(z - z_{\ell} + \Delta_{\ell}^{b})\Theta(z_{\ell} - z + \Delta_{\ell}^{f}), \tag{2.1}$$

where Θ is the Heaviside function. Here, $\Delta_{\ell}^{f/b}$ is the distance that the ℓ-th layer extends towards

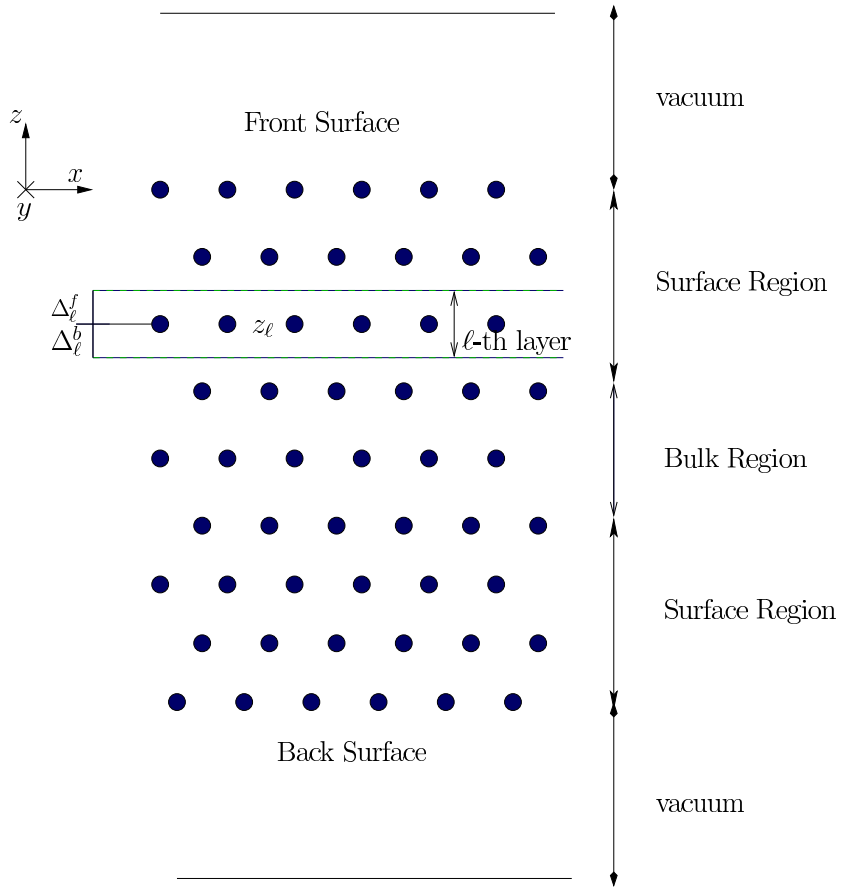

Figure 2.1: (color on line) A sketch of the super-cell. The atomic slab corresponds to the circles representing the atoms of the system.

the front (f) or back (b) from its z_ℓ position. We take z_ℓ to be at the center of an atom that belongs to layer ℓ, so the previous equation would give the ℓ-th atomic-layer contribution to the nonlinear optical response. $\Delta_\ell^f + \Delta_\ell^b$ is the thickness of layer ℓ (see Fig. 2.1).

To introduce the cut function $\mathcal{C}(z)$ in the calculation of nonlinear optical susceptibility $\chi^{\rm abc}$, we start from the operator for the electron current, $\mathbf{j}(\mathbf{r}) = \frac{e}{2}\left(\mathbf{v}^\Sigma|\mathbf{r}\rangle\langle\mathbf{r}| + |\mathbf{r}\rangle\langle\mathbf{r}|\mathbf{v}^\Sigma\right)$, that leads to

$$\mathbf{j}^{(2)}(\mathbf{r},t) = \mathrm{Tr}(\mathbf{j}(\mathbf{r})\rho^{(2)}(t)) = \int \frac{dk^3}{8\pi^3}\sum_{nm}\rho^{(2)}_{nm}(\mathbf{k};t)\mathbf{j}_{mn}(\mathbf{k};\mathbf{r}), \tag{2.2}$$

where

$$\mathbf{j}_{mn}(\mathbf{k};\mathbf{r}) = \frac{e}{2}\left(\langle m\mathbf{k}|\mathbf{v}^\Sigma|\mathbf{r}\rangle\langle\mathbf{r}|n\mathbf{k}\rangle + \langle m\mathbf{k}|\mathbf{r}\rangle\langle\mathbf{r}|\mathbf{v}^\Sigma|n\mathbf{k}\rangle\right). \tag{2.3}$$

We have used the one electron density operator ρ, with which we can calculate the expectation value of a single-particle observable $\mathcal{O}$ as $\langle\mathcal{O}\rangle = \mathrm{Tr}(\rho\mathcal{O})$, with $\mathcal{O}$ the associated quantum mechanical operator and Tr the trace. We have introduced $\mathbf{v}^\Sigma_{nm}(\mathbf{k})/i\omega^\Sigma_{nm}(\mathbf{k}) = \mathbf{r}_{nm}(\mathbf{k})$, this corresponds to the

matrix elements of the position operator in reciprocal space, which can be written using the one electron velocity operator with the scissors correction $\mathbf{v}^{\Sigma}$, needed to have the correct value of the energy band gap due to the DFT-LDA underestimation of this value.

Integrating the microscopic current $\mathbf{j}(\mathbf{r},t)$ over the entire slab gives the averaged microscopic current density, $\mathbf{J}(t)$. If we want the contribution from only one region of the unit cell towards the total current, we can integrate $\mathbf{j}(\mathbf{r},t)$ over the desired region. Then the contribution to the current density from the chosen region of the slab is given by

$$\frac{1}{A}\int d^3r\, \mathcal{C}(z)\, \mathbf{J}^{(2)}(\mathbf{r},t) \equiv \boldsymbol{\mathcal{J}}^{(2)}(t),$$

where $\boldsymbol{\mathcal{J}}^{(2)}(t)$ is the 2nd order current induced in the region specified by $\mathcal{C}(z)$. For the case of SHG, the perturbation theory with the electric field as perturbation has to be taken at least to 2nd order [13]. Therefore we define

$$e\boldsymbol{\mathcal{V}}^{\Sigma}_{mn}(\mathbf{k}) \equiv \int d^3r\, \mathcal{C}(z)\, \mathbf{j}_{mn}(\mathbf{k};\mathbf{r}), \tag{2.4}$$

to write the Fourier transform of equation (2.2) as

$$\boldsymbol{\mathcal{J}}^{(2)}(2\omega) = \frac{e}{A}\int \frac{dk^3}{8\pi^3}\sum_{mn}\boldsymbol{\mathcal{V}}^{\Sigma}_{mn}(\mathbf{k})\rho^{(2)}_{nm}(\mathbf{k};2\omega), \tag{2.5}$$

that gives the induced microscopic current of the chosen region, to order 2 in the external perturbation. From Eqs. (2.4) and (2.3) we obtain

$$\begin{aligned}
\boldsymbol{\mathcal{V}}^{\Sigma}_{mn}(\mathbf{k}) &= \frac{1}{2}\int \mathrm{d}^3r\, \mathcal{C}(z)\Big[\langle m\mathbf{k}|\mathbf{v}^{\Sigma}|\mathbf{r}\rangle\langle\mathbf{r}|n\mathbf{k}\rangle + \langle m\mathbf{k}|\mathbf{r}\rangle\langle\mathbf{r}|\mathbf{v}^{\Sigma}|n\mathbf{k}\rangle\Big] \\
&= \frac{1}{2}\int \mathrm{d}^3r\, \mathcal{C}(z)\Big[\psi_{n\mathbf{k}}(\mathbf{r})\mathbf{v}^{\Sigma *}\psi^{*}_{m\mathbf{k}}(\mathbf{r}) + \psi^{*}_{m\mathbf{k}}(\mathbf{r})\mathbf{v}^{\Sigma}\psi_{n\mathbf{k}}(\mathbf{r})\Big] \\
&= \int \mathrm{d}^3r\, \psi^{*}_{m\mathbf{k}}(\mathbf{r})\left[\frac{\mathcal{C}(z)\mathbf{v}^{\Sigma} + \mathbf{v}^{\Sigma}\mathcal{C}(z)}{2}\right]\psi_{n\mathbf{k}}(\mathbf{r}) \\
&= \int \mathrm{d}^3r\, \psi^{*}_{m\mathbf{k}}(\mathbf{r})\boldsymbol{\mathcal{V}}^{\Sigma}\psi_{n\mathbf{k}}(\mathbf{r}),
\end{aligned}$$

where, we used the hermitian property of $\mathbf{v}^{\Sigma}$ and defined

$$\boldsymbol{\mathcal{V}}^{\Sigma} = \frac{\mathcal{C}(z)\mathbf{v}^{\Sigma} + \mathbf{v}^{\Sigma}\mathcal{C}(z)}{2}.$$

We see that the replacement

$$\mathbf{V} \to \boldsymbol{\mathcal{V}} = \frac{\mathcal{C}(z)\mathbf{V} + \mathbf{V}\mathcal{C}(z)}{2}, \tag{2.6}$$

is all that is needed to change any occurrence of the one electron velocity operator $\mathbf{V}$ to the new velocity operator $\boldsymbol{\mathcal{V}}$ that implicitly takes into account the contribution of the region of the slab given by $\mathcal{C}(z)$. We note that this modified operator is hermitian as it should [39]. and if we take

$\mathcal{C}(z) = 1$ through out, the layered matrix elements $\boldsymbol{\mathcal{V}}^{\Sigma}_{nm}$ become standard bulk-like $\mathbf{V}^{\Sigma}_{nm}$ matrix elements.

Finally, we could also calculate the nonlinear surface susceptibility as

$$\boldsymbol{\chi}(-2\omega;\omega,\omega) = \sum_{\{\ell\}} \boldsymbol{\chi}^{\ell}(-2\omega;\omega,\omega), \tag{2.7}$$

where ℓ would denote a particular layer chosen through $\mathcal{C}^{\ell}(z)$ of equation (2.1) and $\{\ell\}$ is meant to be a chosen set of layers. For instance, one can take a single layer encompassing half of the slab, or take each atomic layer individually to the middle of the slab. For the first case there is a single summand in equation (2.7). For the second case there is a sum from $\ell = 1$, denoting the first layer right at the surface, to $\ell = N$, denoting the layer at the middle of the slab.

2.2 SHG response

The SHG intensity for a given incidence of the electrical field depends of the elements of the χ^{abc} tensor. Mathematically this is a third rank tensor with 2ω dependence and complex values. From now on we will refer to it as $\chi^{abc}(2\omega)$. The nonlinear second order susceptibility can be written in terms of the resonant contribution of transitions at frequency ω and 2ω [31]:

$$\chi^{\mathrm{abc}}(2\omega) = \chi^{\mathrm{abc}}_{e,\omega}(2\omega) + \chi^{\mathrm{abc}}_{e,2\omega}(2\omega) + \chi^{\mathrm{abc}}_{i,\omega}(2\omega) + \chi^{\mathrm{abc}}_{i,2\omega}(2\omega). \tag{2.8}$$

In the last equation the subindex e denotes the contribution from intraband transitions and i from interband transitions.

For the numerical calculation of the SHG response the nonlinear susceptibility tensor components are given by [31]:

$$\mathrm{Im}[\chi^{\mathrm{abc}}_{e,\omega}] = \frac{\pi|e|^3}{2\hbar^2}\int\frac{dk^3}{8\pi^3}\sum_{vc}\sum_{q\neq(v,c)}\frac{1}{\omega^{\Sigma}_{cv}}\left[\frac{\mathrm{Im}[\mathcal{V}^{\Sigma,\mathrm{a}}_{qc}\{r^{\mathrm{b}}_{cv}r^{\mathrm{c}}_{vq}\}]}{(2\omega^{\Sigma}_{cv}-\omega^{\Sigma}_{cq})} - \frac{\mathrm{Im}[\mathcal{V}^{\Sigma,\mathrm{a}}_{vq}\{r^{\mathrm{c}}_{qc}r^{\mathrm{b}}_{cv}\}]}{(2\omega^{\Sigma}_{cv}-\omega^{\Sigma}_{qv})}\right]\delta(\omega^{\Sigma}_{cv}-\omega), \tag{2.9a}$$

$$\mathrm{Im}[\chi^{\mathrm{abc}}_{i,\omega}] = \frac{\pi|e|^3}{2\hbar^2}\int\frac{dk^3}{8\pi^3}\sum_{cv}\frac{1}{(\omega^{\Sigma}_{cv})^2}\left[\mathrm{Re}\left[\left\{r^{\mathrm{b}}_{cv}\left(\mathcal{V}^{\Sigma,\mathrm{a}}_{vc}\right)_{;k^{\mathrm{c}}}\right\}\right] + \frac{\mathrm{Re}\left[\mathcal{V}^{\Sigma,\mathrm{a}}_{vc}\left\{r^{\mathrm{b}}_{cv}\Delta^{\mathrm{c}}_{cv}\right\}\right]}{\omega^{\Sigma}_{cv}}\right]\delta(\omega^{\Sigma}_{cv}-\omega), \tag{2.9b}$$

$$\mathrm{Im}[\chi^{\mathrm{abc}}_{e,2\omega}] = -\frac{\pi|e|^3}{2\hbar^2}\int\frac{dk^3}{8\pi^3}\sum_{vc}\frac{4}{\omega^{\Sigma}_{cv}}\left[\sum_{v'\neq v}\frac{\mathrm{Im}[\mathcal{V}^{\Sigma,\mathrm{a}}_{vc}\{r^{\mathrm{b}}_{cv'}r^{\mathrm{c}}_{v'v}\}]}{2\omega^{\Sigma}_{cv'}-\omega^{\Sigma}_{cv}} - \sum_{c'\neq c}\frac{\mathrm{Im}[\mathcal{V}^{\Sigma,\mathrm{a}}_{vc}\{r^{\mathrm{c}}_{cc'}r^{\mathrm{b}}_{c'v}\}]}{2\omega^{\Sigma}_{c'v}-\omega^{\Sigma}_{cv}}\right]\delta(\omega^{\Sigma}_{cv}-2\omega), \tag{2.9c}$$

$$\mathrm{Im}[\chi^{\mathrm{abc}}_{i,2\omega}] = \frac{\pi|e|^3}{2\hbar^2}\int\frac{dk^3}{8\pi^3}\sum_{vc}\frac{4}{(\omega^{\Sigma}_{cv})^2}\left[\mathrm{Re}\left[\mathcal{V}^{\Sigma,\mathrm{a}}_{vc}\left\{\left(r^{\mathrm{b}}_{cv}\right)_{;k^{\mathrm{c}}}\right\}\right] - \frac{2\mathrm{Re}\left[\mathcal{V}^{\Sigma,\mathrm{a}}_{vc}\left\{r^{\mathrm{b}}_{cv}\Delta^{\mathrm{c}}_{cv}\right\}\right]}{\omega^{\Sigma}_{cv}}\right]\delta(\omega^{\Sigma}_{cv}-2\omega), \tag{2.9d}$$

For this set of equations $\mathrm{Im}[\chi^{\mathrm{abc}}_{i,\omega}]$ is the imaginary part of the nonlinear optical susceptibility for the SHG at a frequency ω and due to interband transitions, whilst $\chi^{\mathrm{abc}}_{e,2\omega}$ is the contribution

to the SHG from intraband transitions. The constant e is the fundamental charge and the $\int dk^3$ corresponds to an integration on the first Brillouin zone. The factors $\hbar\omega_{cv}^{\sigma}$ are the energy difference between the c and v state of the system after the scissors correction. The factor $\mathcal{V}_{vc}^{\Sigma,\mathrm{a}}$ are the matrix elements of the electron velocity operator for the a Cartesian index, with the cut function applied for a given layer and with the scissors correction, this is a rigid correction to the band structure gap due to the DFT underestimation of this value, this value is usually taken from an experimental measurement or a GW calculation. The factors r_{cv}^{b} are the matrix elements of the position operator for the b-th Cartesian index.

The real part of each contribution can be obtained through a Kramers-Kronig transformation [40] and to fulfill the required intrinsic permutation symmetry, the $\{\}$ notation symmetrizes the bc Cartesian indices, i.e. $\{u^{\mathrm{b}}s^{\mathrm{c}}\} = (u^{\mathrm{b}}s^{\mathrm{c}} + u^{\mathrm{c}}s^{\mathrm{b}})/2$, and thus $\chi^{\mathrm{abc}} = \chi^{\mathrm{acb}}$.

3 Methodology

Outline

In this chapter we will show the scheme for the calculation of the SHG response. Then we will explain about the defects and misfits that will be induced in the crystalline lattice.

The SHG response was calculated using the TINIBA [41] code. TINIBA was developed at the Centro de Investigaciones en Optica, A.C., it is a suite of scripts that works with the ABINIT [42] package to run and calculate optical properties of crystalline semiconductors by parallelizing the computation of the different quantities involved in the procedure. It is written primarily in FORTRAN with Bash wrapper scripts. TINIBA can calculate the SHG response using the length formalism and the expressions in (2.9), but SHG has a higher sensitivity to the crystalline cell deformations due to its noncentrosymmetry dependence. For the calculation of the SHG response in (2.8), the self-consistent ground state and the Kohn-Sham states were calculated in the DFT-LDA framework using the plane-wave ABINIT code [42]. We used Troullier-Martins pseudopotentials [43] that are fully separable nonlocal pseudopotentials in the Kleinman-Bylander form [44].

The vacuum size in the figure 2.1 is equivalent to one quarter the size of the slab, avoiding the effects produced by possible wave-function tunneling from the contiguous surfaces of the full crystal formed by the repeated super-cell scheme [37].

Spin-orbit, local field, and electron-hole attraction [45] effects on the SHG process are all neglected. Although these are important factors in the optical response of a semiconductor, their efficient calculation is still theoretically and numerically challenging and under debate. This merits further study but is beyond the scope of this thesis. For a given slab size, we find the converged spectra to obtain the relevant parameters. The most important of these are: an energy cut-off of 10 Ha for the layered slabs, an equal number of conduction and valence bands, and a set of 630 **k**-points. The **k**-points are used for the linear analytic tetrahedron method for evaluating the 3D Brillouin Zone (BZ) integrals where special care was taken to examine the double resonances of Eq. (2.9) [24] that arises due to the high density of states of the resonances. Note that the Brillouin zone for the slab geometry collapses to a 2D-zone, with only one **k**-point along the z-axis for thin

slabs. All spectra were calculated with a Gaussian smearing of 0.15 eV. This value has the best concordance with experimental measurements [31].

3.1 System of study

Due to the theoretical and computational complications for the first principles calculations in ferroelectric materials, we chose Gallium Arsenide 2D slabs with their main surface in the (110) direction. This 2D material can be fabricated using several experimental techniques such as clevage of bulk GaAs [46–48].

This GaAs(110) slab is useful for nonlinear optics experiments because like ferroelectric materials, it is a noncentrosymmetric material. It will have a natural SHG response and this will be useful to measure SHG differences when the noncentrosymmetry of the material is altered. From now on we will refer to the natural material response as the relaxed case response. Bulk GaAs has a Zinc-Blende structure, it is formed by two face centered cube structures with one displaced to 1/4 from the other in the main diagonal. The atoms are tetrahedrally coordinated with 108° bonds.

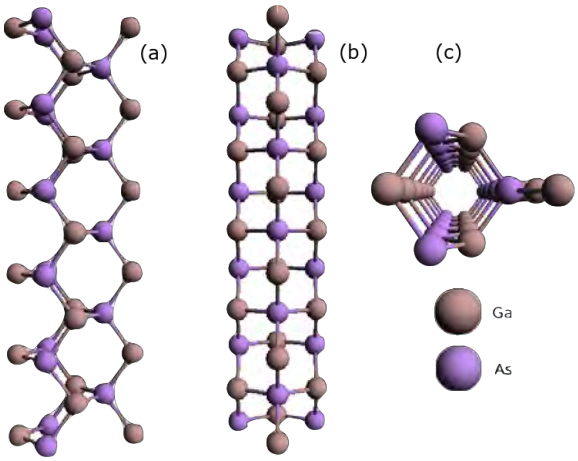

Figure 3.1: GaAs slab cell in the (a) x, (b) y and (c) z direction.

For the construction of the periodic cell we used 11 layers of material, each layer containing a Ga and a As atom. This is shown in figure 3.2. The material has been relaxed to minimize the system energy because of the finite size of the slab in the z direction. A vacuum in the z direction was included and due to the periodicity of the cell the vacuum will separate the different slabs. Also, the vacuum in the z direction needs to be large enough so that the wavefunctions of the different slabs can not overlap [31].

3.2 Induced defects

For the GaAs(110) slabs we will add two kinds of defects. The first one consist in a small displacement of a Ga or As atom in the cell. As a result of the periodicity in the cell, this defect will

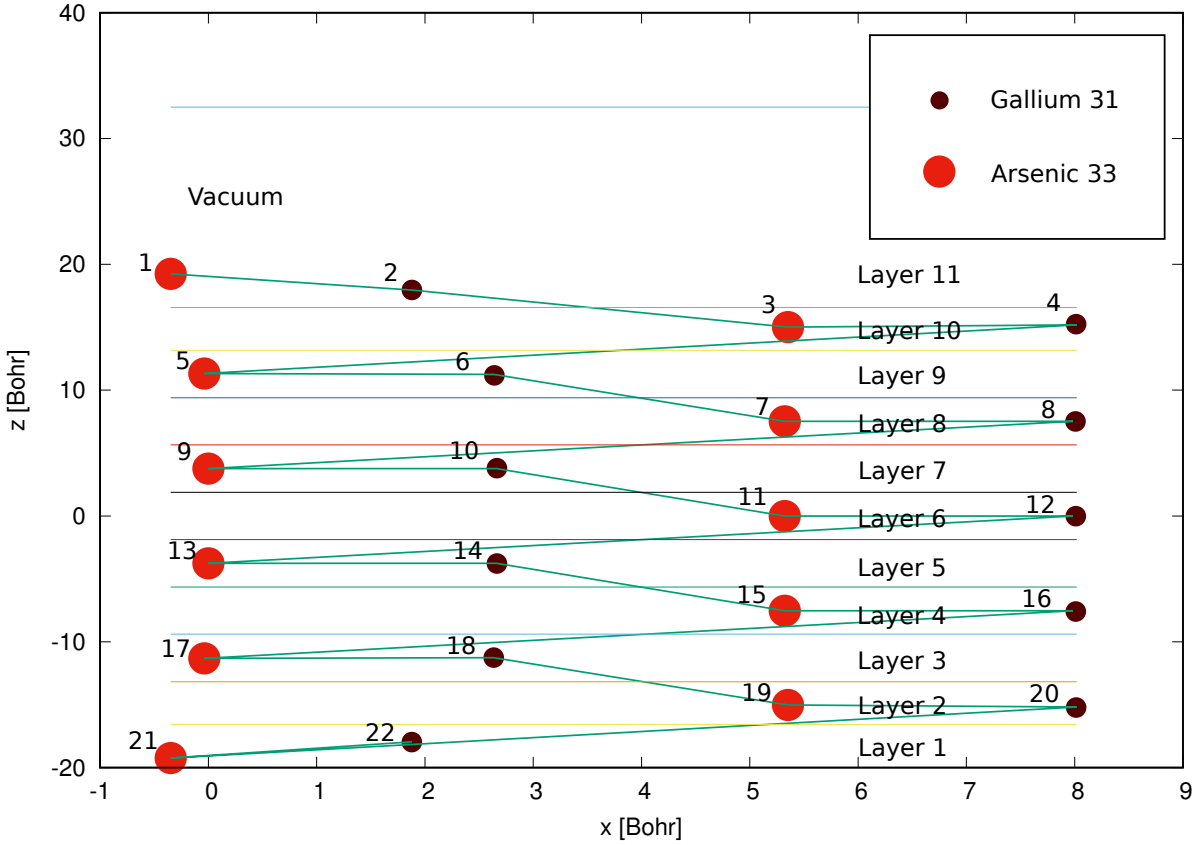

Figure 3.2: Periodic Cell for the GaAs slab with all the atoms in their relaxed position. Each layer contains a Ga and a As atom and each has a label at its left.

become periodic. The atom will be moved above and bellow its equilibrium position, giving us a measure of the change in the SHG response for each one of its positions. The second kind of defect is called misfit, this is a dislocation that we will create by displacing the lower half of the slab in the x direction. This defect will emulate the mismatch that could arise in the interface of buried materials when one of the films in under a strain induced relaxation like the buried ferroelectric surfaces in reference [2].

For the periodical displacement of an atom in the cell, the displacement will be induced for all the atoms in the lower half of the slab cell, namely, Ga and As atoms contained between layers 1 to 6, having each calculation only one atom of the displaced in the periodic cell. The range of displacement is defined as 10% of the width of the current layer. For this system this distance is less

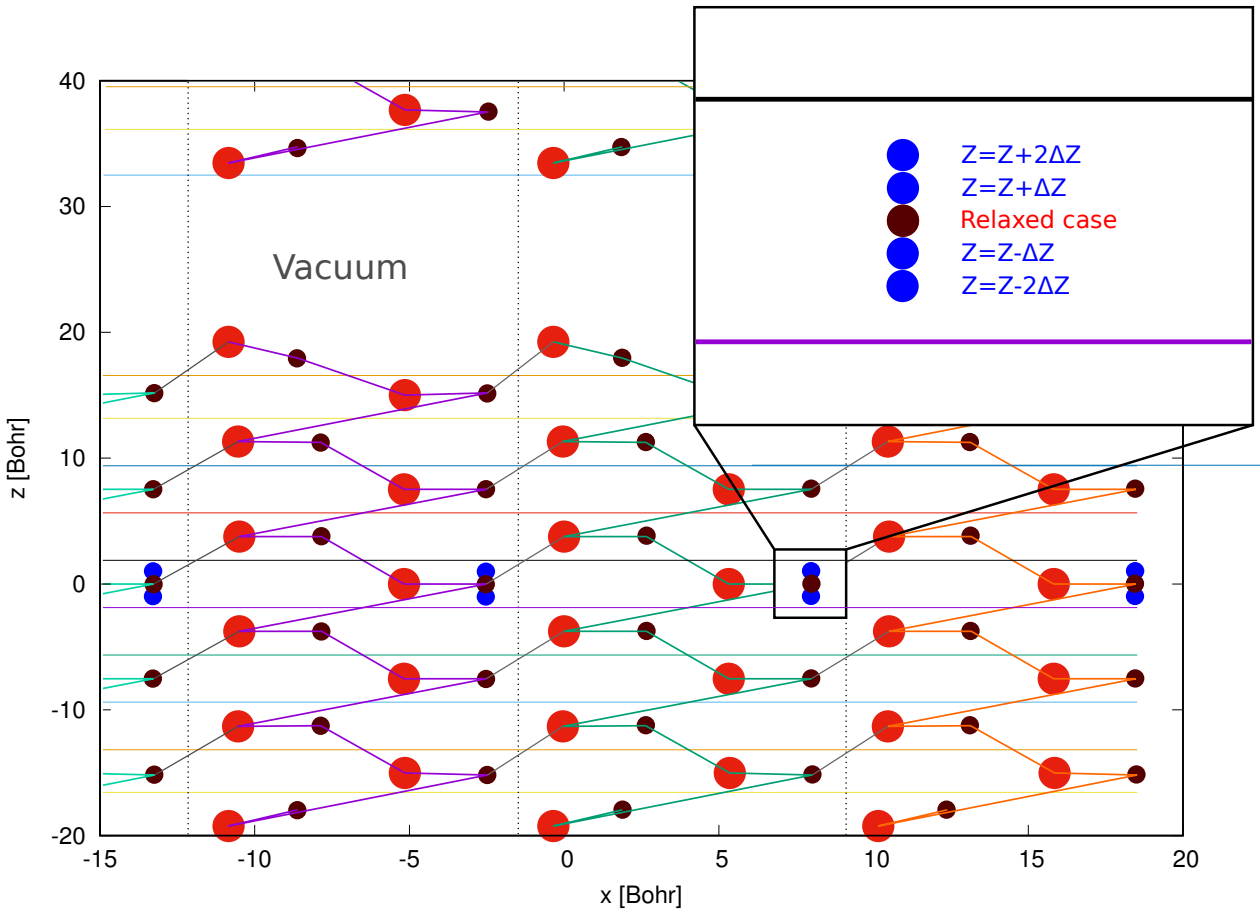

Figure 3.3: Scheme for the periodical displacement of an atom: each colored circle corresponds to a relaxed atomic position whilst blue colored circles are the displacements for the selected atom.

than 1Bohr and it has been divided into six steps. A schematic representation of these displacements is shown in figure 3.3 for the central atom of the crystal. In this figure the relaxed slab cell has been repeated three times in the x direction and the lower part of the next slab can be seen above z = 30.

For the calculation of the second kind of defect, the misfit, all the atoms in that lower half were displaced in the negative x direction a 5% of the average atomic distance in that direction, this displacement was divided into six steps. A scheme of the misfit is shown in figure 3.4.

The displacement induced in the figure 3.4 will give us the SHG response corresponding to the stack of two slabs of GaAs(110) with a mismatch produced by a noncontinuous deposition, strain

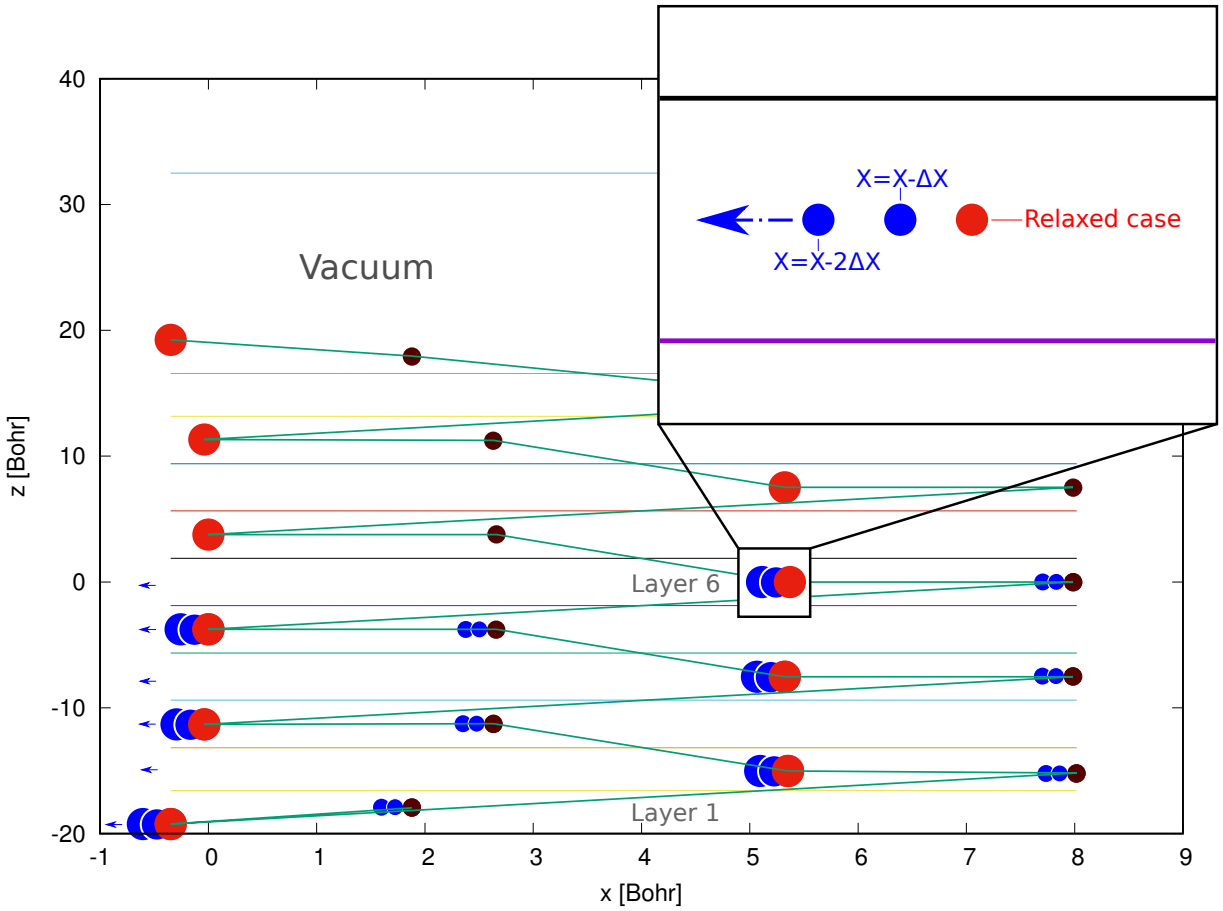

Figure 3.4: Half slab misfit scheme: all the atoms of the lower half of the slab have been displaced towards $-x$ direction.

or staking in vacuum.

To get an ordered calculation of this defects a Bash / C++ console application was developed; this script uses the files required for the relaxed case calculation as an input, and automatically generates the cases for each displacement of the selected atoms or misfits. After the input generation, all the cases can be run in parallel using TINIBA via the application scripts.

4 Calculation results and analysis

Outline

All calculation in this thesis were accomplished using the CIO supercomputer MEDUSA, during 6 months of calculations using 12 nodes, each with 12 cores at 3.46 GHz. Visualization of the unitary cells and slabs were done using Avogadro and Gnuplot.

In this chapter we will present the results of the calculation for the SHG responses and the method for the analysis of the induced defects in the GaAs(110) slabs. For the nonlinear susceptibility $\chi^{abc}(2\omega)$ we will have 27 components: 9 will be zero due to the SHG permutation properties. Some of the other 18 components will be near equal to zero due to the system properties and some will have higher intensity. The tensor components that represent the P polarization will involve a z component, they will represent perpendicular incidence of the electric field and will not be used because of the difficulty to simulate the field screening at the surface of the material. A scheme for the P and S polarization of the electric field is shown in figure 4.1.

To select the components to work with, previous calculations were ran for all the possible nonzero tensor components that can represent the S polarization incidence. The xxx, xyy and yxy components were chosen due to its high intensity. The previous calculations also showed that the higher intensity components had a higher variation in the amplitude of the SHG signal due to the defects.

4.1 $\chi^{abc}(2\omega)$ surface calculation

For the selected tensor components we converged the calculations for the relaxed case and found that most of the peaks that could arise into optical activity were in range of $[0, 4]$ eV. From equation (2.7), the calculated intensity $|\chi^{abc}(2\omega)|$ of the selected components is shown in figure 4.2.

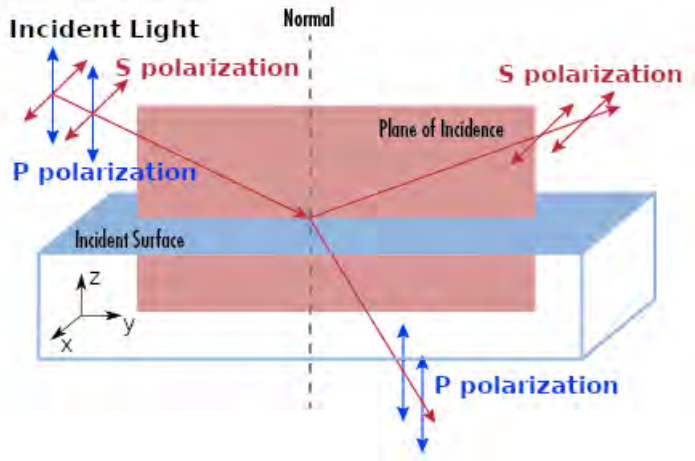

Figure 4.1: Incidence diagram for the P and S polarization of the electric field.

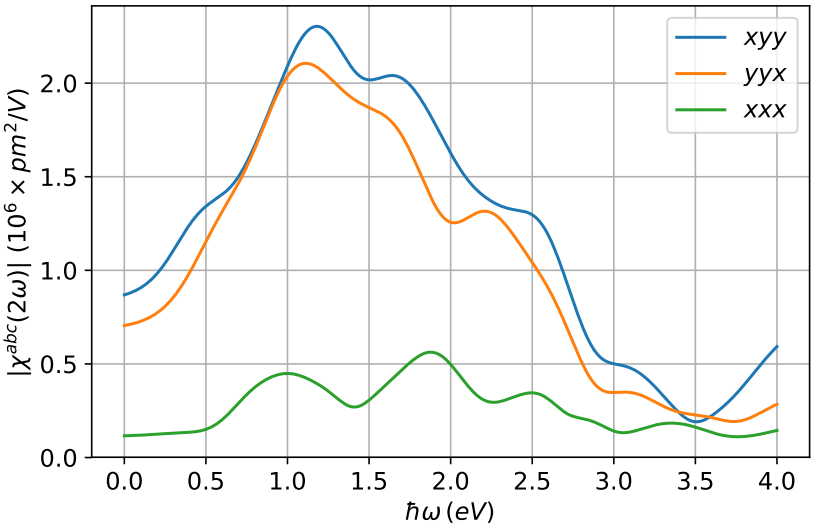

Figure 4.2: Strongest components of $|\chi^{abc}(2\omega)|$ for the GaAs110 surface response; $\hbar\omega$ represents the one photon energy.

The SHG response of the material will depend on the value of the components of $|\chi^{abc}(2\omega)|$ at twice the energy of the incident field. For a Ti:sapphire laser with a energy peak at 1.55 eV the efficiency of the SHG will be related to the $|\chi^{abc}(2\omega)|$ values at 3.1 eV.

The intensity of the SHG signal will change in different way for each displacement, tensor component and frequency of the incident field. There are also regions in the spectrum that have a higher amplitude in the signal, which can be useful for experimental comparisons. To facilitate the analysis, we will represent in which regions of the spectrum, the SHG signal for each displacement

will deviate the most. A wider variation for a given frequency will allow us to know by comparison which atom of the periodic cell has been displaced and its location. For this we will introduce the $D^{abc}(2\omega)$ function:

$$D^{abc}(2\omega) = (|\chi^{abc}_{displ}(2\omega)|)^2 - (|\chi^{abc}_{relax}(2\omega)|)^2. \tag{4.1}$$

In equation (4.1) $D(2\omega)$ represents the difference between the squares of the measured component of the material in the relaxed case and the material with the induced displacement. This choice was not arbitrarily, during the analysis we used differences between the components, squared differences, and the difference of the squared components was the quantity that allowed to identify easier the different defects.

By using the values of the nonlinear susceptibility we would be able to distinguish which atom of the crystalline slab has been displaced; lets suppose that for the GaAs110 slab, the center atom zoomed in the figure 3.3 has been displaced -1.9×10^{-1} Bohr in the z direction, we would have a notorious difference with the nonlinear response of the relaxed case, this difference is shown in 4.3 (a), these squared subtractions are always different for each atom and for each displacement, as can be seen in figure 4.3 (b) for the 15-th As atom, which is below the 11-th As atom in figure 3.3 and has been displaced 1.9×10^{-1} Bohr upward.

4.2 $\chi^{abc}(2\omega)$ layered calculation

By using the cut function formalism we calculated the response for each layer of the slab for all displacement cases. This layered responses allow us to analyse only the SHG signal contribution that comes from a given layer.

The higher variations in the $|\chi^{abc}(2\omega)|$ spectra came from the either the layer in which the atom was displaced or in the adjacent layer in the direction of atomic displacement. This behaviour was found in the three tensor components that were analyzed. Two examples are shown in figure 4.4: the layer 6 in (a) has the highest response and it contains the 11-th atom which has been displaced. However, if there is a displaced atom in another layer, the higher peak in $D^{abc}(2\omega)$ will come from that layer due to the noncentrosymmetry breaking. This is shown in (b), where the highest intensity comes from the layer 4 that contains the 15-th atom which has been displaced from its equilibrium position. We mention that odd layers were omitted in this figure to improve visualization. As a drawback, to do this layer analysis, we need to determine the SHG response in a wide range of the spectra. This is because the frequency of the higher peak changes with each layer. Thus, to find the higher peak among layers, the experimentalist will have to measure $|\chi^{abc}(2\omega)|$ in the whole optical frequency range.

4.3 Induced variance and energy point analysis

Usually the nonlinear susceptibility is measured experimentally using a Ti:sapphire laser, this is a femtosecond laser with a high intensity and an energy peak at 1.55 eV, so the SHG response will be centered at 3.1 eV. We can also see from figure 4.2 that the higher response for the components spectra is located around 1.2 eV. Is convenient to introduce a method to estimate the variation of

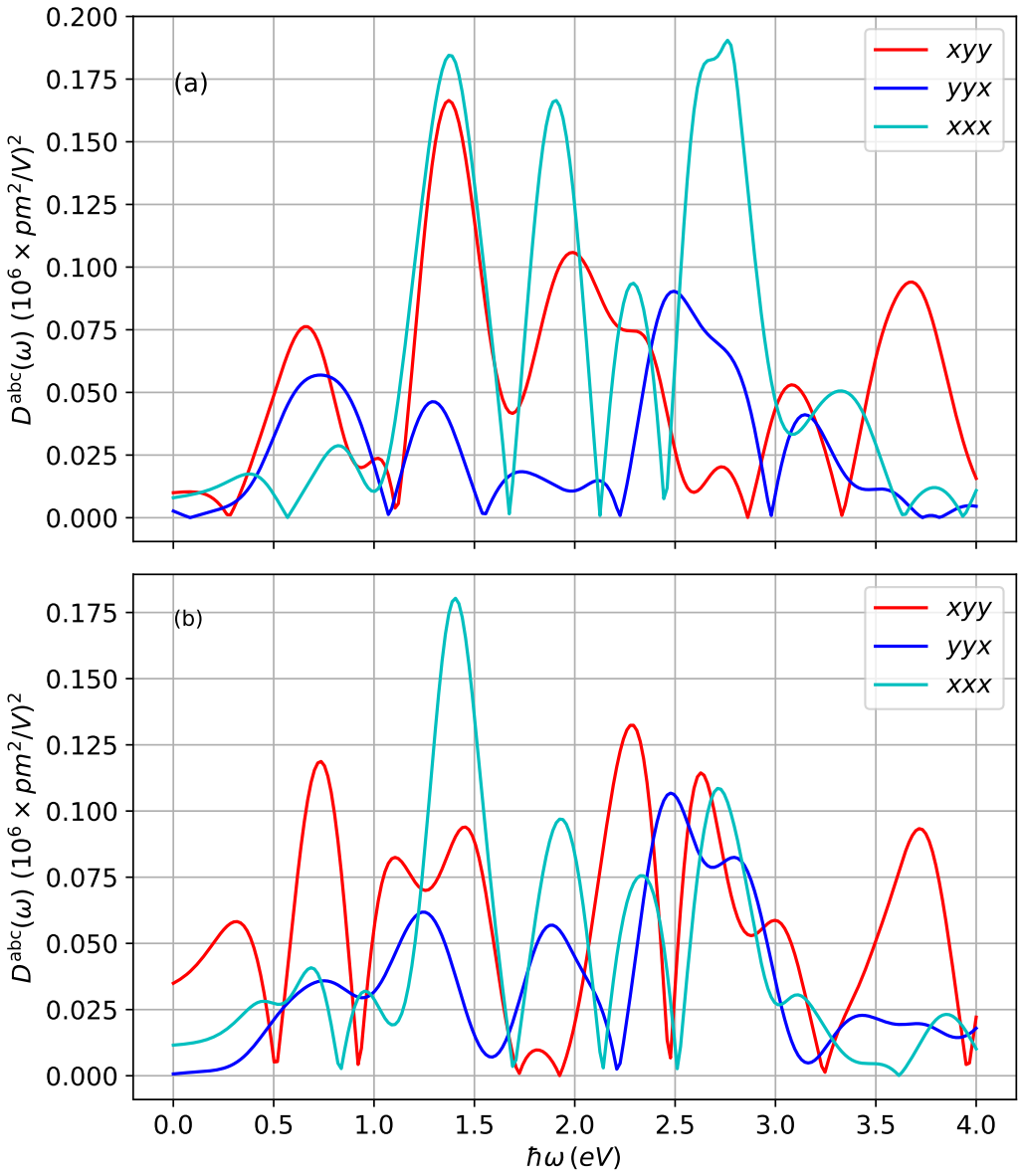

Figure 4.3: Difference between the squared components of $|\chi^{abc}(2\omega)|$ for the minimum displacements of the (a) 11-th and (b) 15-th atom.

the SHG response from case to case. we will introduce a statistical variance for the changes in the nonlinear response due to the displacements of an atom in the periodic cell:

$$\sigma^{abc}(2\omega) = \frac{\sum_{i=1}^{N}(|\chi^{abc}_{relax}(2\omega)| - |\chi^{abc}_{i-displ}(2\omega)|)^2}{N}. \tag{4.2}$$

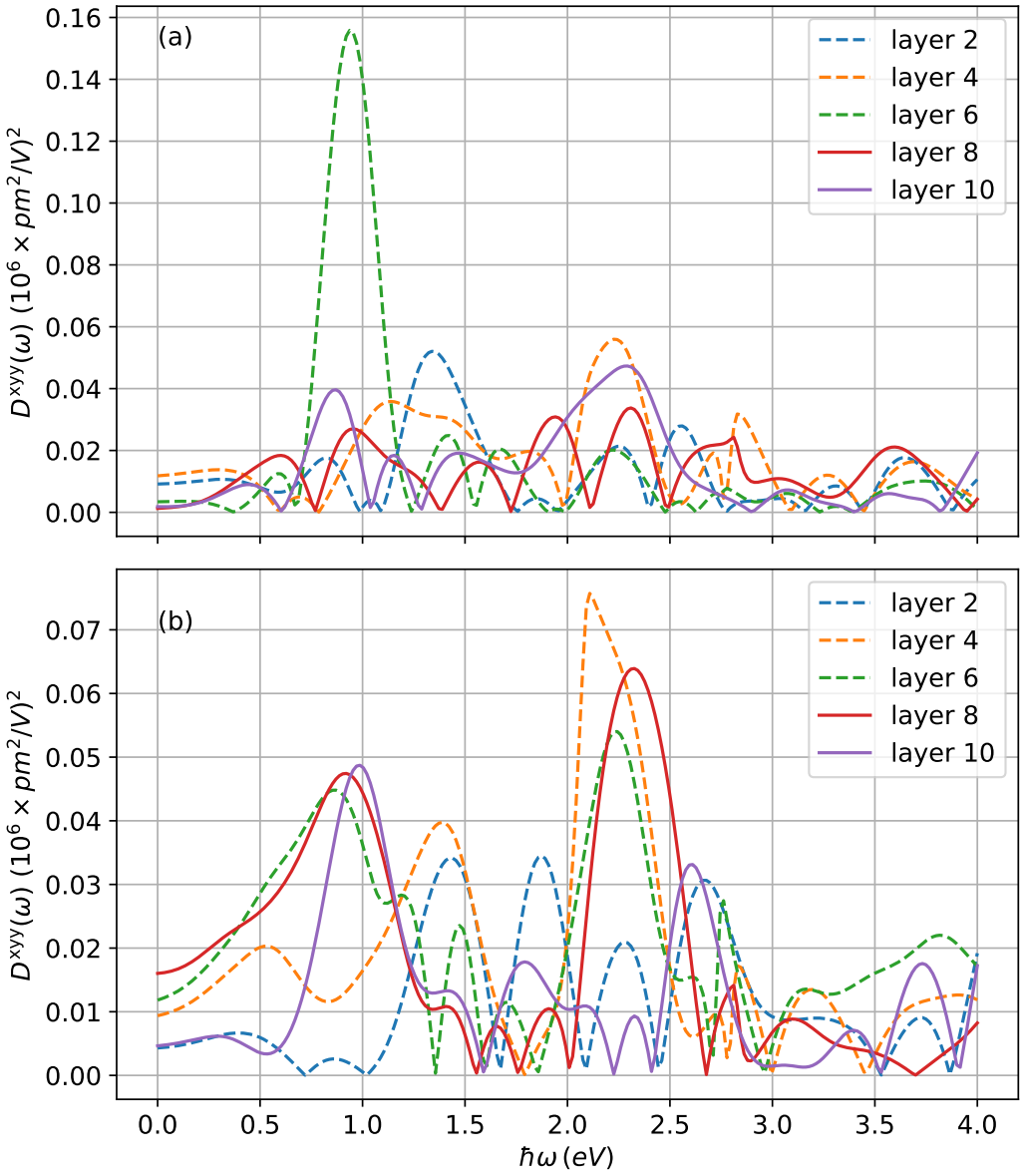

Figure 4.4: Layered SHG difference for the (a) 11-th atom displaced in layer 6 and the (b) 15-th atom displaced in layer 4. The higher variation comes from the layer with the displaced atom.

Where $|\chi^{\text{abc}}_{i-\text{displ}}(2\omega)|$ is the intensity of the SHG response for the i-th displacement of the given atom, $|\chi^{\text{abc}}_{\text{relax}}(2\omega)|$ is the relaxed case SHG intensity and N the number of displacements calculated for the atom. $\sigma^{\text{abc}}(2\omega)$ will be a measurement of the dispersion in the intensity of a $|\chi^{\text{abc}}|$ tensor component for the displacements of an atom and for a given frequency of the incident field. The

main objective is to separate the displacements using its difference with the relaxed case. If the intensities have a wider scatter, they will be easier to identify. Thus, the variance will give us a measure of the easiness to identify the atom position for each frequency.

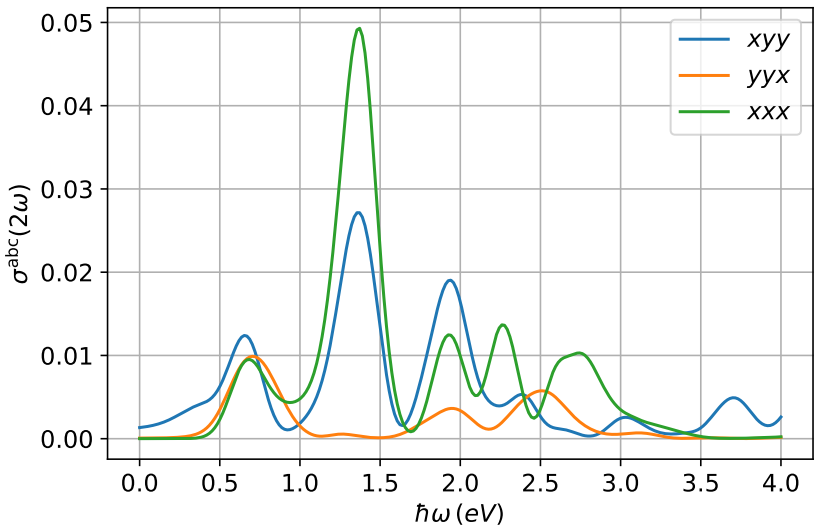

Figure 4.5: $\sigma^{abc}(2\omega)$ for the 19-th atom as a function of the output signal energy.

In the figure 4.5 $\sigma^{abc}(3.1\,eV)$ has a low amplitude. This means that the values of the SHG intensity are not widely scattered for this frequency of the SHG. On the other hand, as a result of the high sensitivity of SHG to changes in the noncentrosymmetry, 3.1 eV can still be used to identify the displaced atom in the periodic cell and its displacement, as will be shown in figure4.7.

The figures from 4.7 to 4.9 can be read as follows:

- Each colored line represents an atom of the periodic crystalline cell that has been displaced.
- Each dot of the atom line correspond to a displacement for the current atom. The first point from left to right will correspond to $z = z - 3\Delta z$. The central point is the value for the relaxed case, which is easily identificable as $D^{abc}(3.1\,eV) = 0$. Whilst the last point of the line is the value for the displacement of the atom to $z = z + 3\Delta z$.
- The behaviour for the 11-th atom is always symmetrical for the displacements. This is because it is located in the central layer of the slab.

By taking the results of the measurements for different rotations of the material for S-polarization incidence, the experimentalist can acquire the xxx, xyy and yyx components and do a comparative analysis using the figure 4.7 as follows:

1. The atom and its displacement can be found by comparing the measurements with the results of the figure 4.7 for the tensor components.

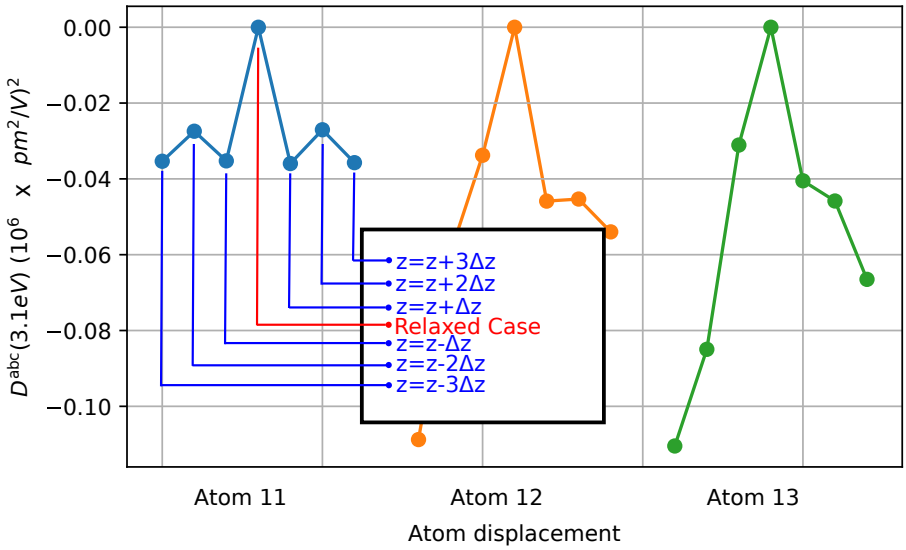

Figure 4.6: Schematic diagram of the representation in figure 4.7.

2. For almost all the atom displacements, the measurements of $D^{\mathrm{abc}}(2\omega)$ are different, so with this three values the defect can be found.

3. If the value is degenerated, like in the case of the displacements of the 11 -th atom (which are the same for $z = z + \Delta z$ and $z = z - \Delta z$), the value of the response for the central layers at 3.1 eV needs to be used, this will give an insight if the atom is displaced upwards or downwards its equilibrium position.

4. The absolute value of the nonlinear susceptibility can also be used to break the degeneracy of the possible atoms and positions. Furthermore, the analysis can be simplified using a tunable laser: if the values of the $|\chi^{\mathrm{xyy}}(2\omega)|$ can be measured in different frequencies, a straightforward algorithm can be implemented to search for the best coincidence between the displaced atoms and their displacements. However, we will focus on this analysis for only a 3.1 eV signal.

Two examples of this process are shown in the figures 4.8 and 4.9, we have two probe cases and the measurements for $D^{\mathrm{abc}}(3.1\,\mathrm{eV})$ from (4.1) for the three selected tensor components. In the two probe cases we marked with black squares all the coincidences for each measurement, and only with a vertical line the ones that match for all three tensor components.

In figure 4.8, for the Ga atom in the 4-th layer labeled as 16, we induced a displacement to the first step below its equilibrium position, $-\Delta z$, after the analysis of the coincidences for measurements shown as a red line, no other atom nor displacement matches the measurement for the three tensor components. For the second probe case the induced defect corresponds to the $+3\Delta z$ step of the 19-th atom, this is the As atom in the 2-th layer. The measurements for the three components are shown as a horizontal green line. Only the values for the selected case matched all the three components. This means that the we have found which has been displaced and its displacement. If there were

two or more atoms and displacements with the same values for the three tensor components, we would not be able to know which has been displaced with this method, yet the intensity of the layered response can be checked. Also, we run a script to know if there are repeated values for the three components of $|\chi^{\mathrm{abc}}(3.1\,\mathrm{eV})|$ in different cases, and we found that there were no repeated values, so each displacement of all the atoms had unique values for the three components, and if needed, more components can be included in the calculation.

The same analysis can be used to search for defects like mismatched buried surfaces, as the lower half slab displacement shown in figure 4.10, the $D^{\mathrm{abc}}(3.1\,\mathrm{eV})$ value for each of the three components of the $|\chi^{\mathrm{abc}}(2\omega)|$ do not cross at the same point at the time, so the experimentalist do not need any information about layer contribution, thus the value of the displacement can be easily obtained by comparison; while this may be true for our calculated values, in case of a degeneracy of the three components (if the three calculated components have the same value of $D^{\mathrm{abc}}(2\omega)$ for different displacements, the absolute value of the tensor can be used to compare instead of squared differences. Doing the same analysis we did the displacement of a single atom in the periodic cell in figures 4.8 and 4.9, we can find the magnitude of the displacement between the cells of two mismatched half slabs, as the misfit case explained in section 3.2. For the figure 4.11, we are comparing the hypothetical measurement results of the tensor components for a displacement of $-3.5\Delta x$ we can see that the only coincidence for the proposed values of the measurement is at a displacement of $-3.5\Delta x$.

Finally, by means of the previous analysis the viability of using the SHG to analyze the morphology of the crystals with ordered defects is shown, especially in the case of misfits. Furthermore this proposed technique for the analysis of slab displacements can be experimentally corroborated creating thin slabs of material by molecular beam epitaxy and staking the slabs together.

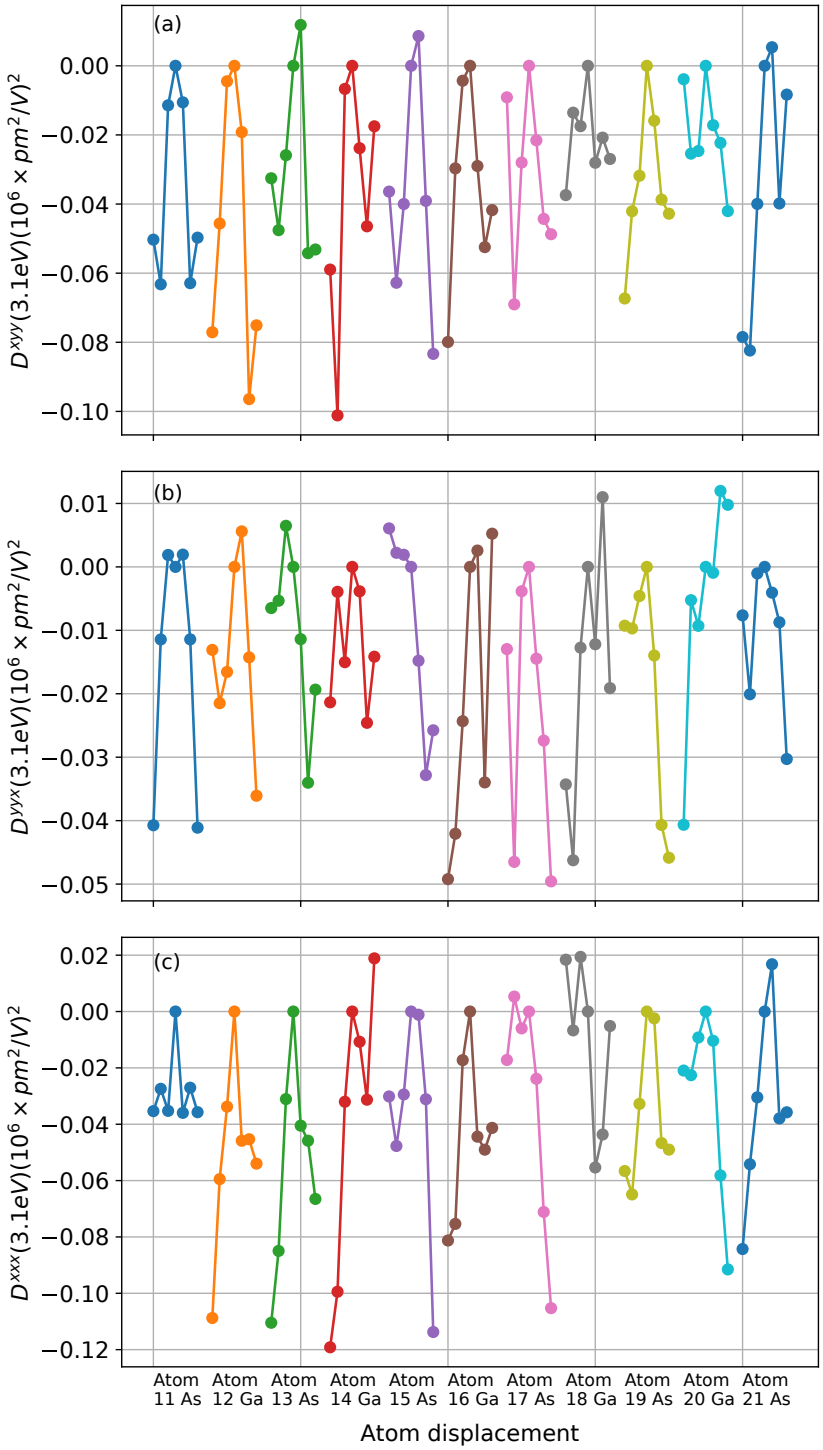

Figure 4.7: Difference of the squared SHG response for each atom and its displacements. The $|\chi^{xyy}(2\omega)|$ component is represented in the section (a) of the panel, $|\chi^{yyx}(2\omega)|$ in section (b) and $|\chi^{xxx}(2\omega)|$ in (c).

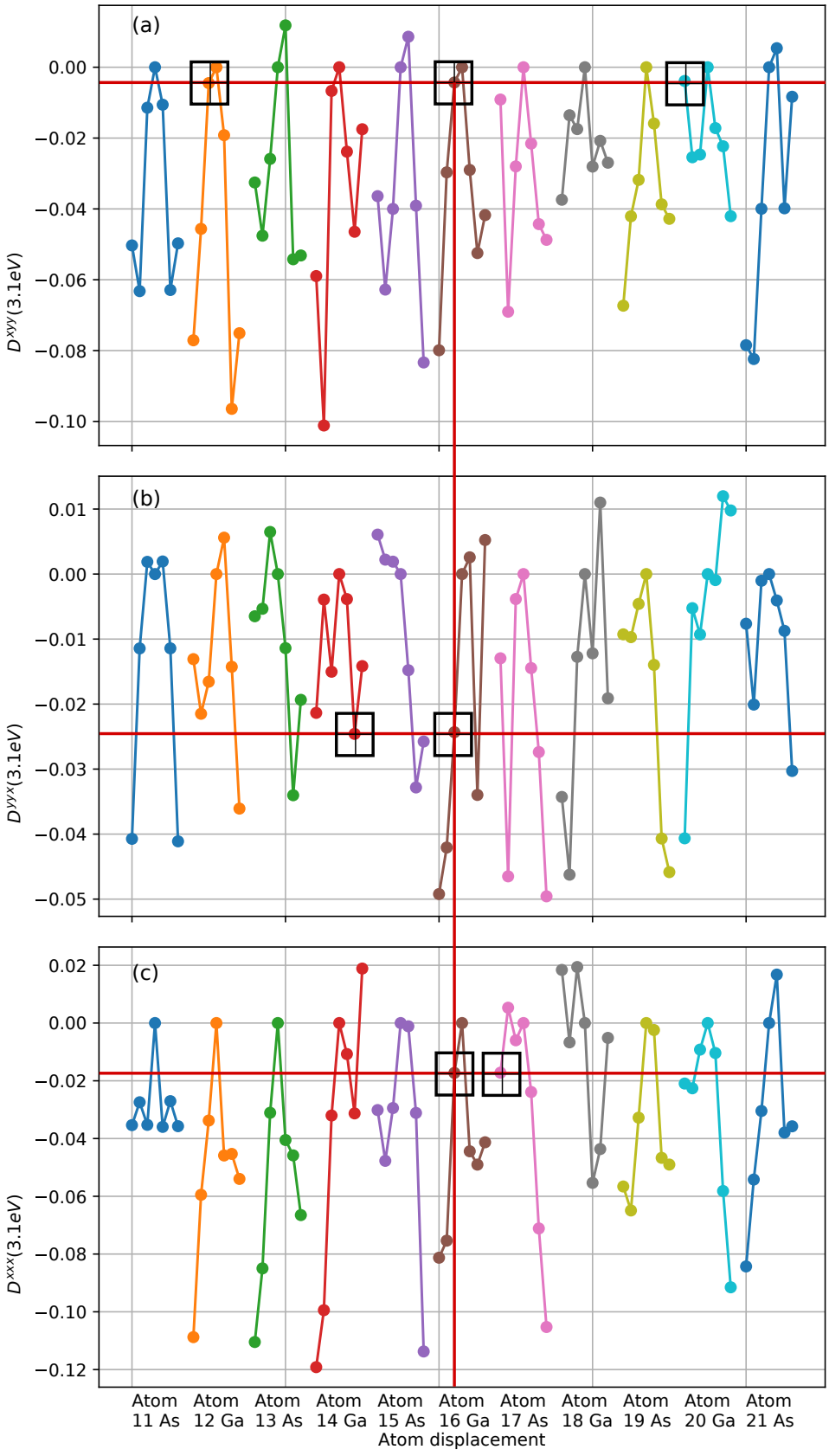

Figure 4.8: Measurement example for a displacement in the 16-th (red horizontal line) atom. Coincidences are marked as black boxes.

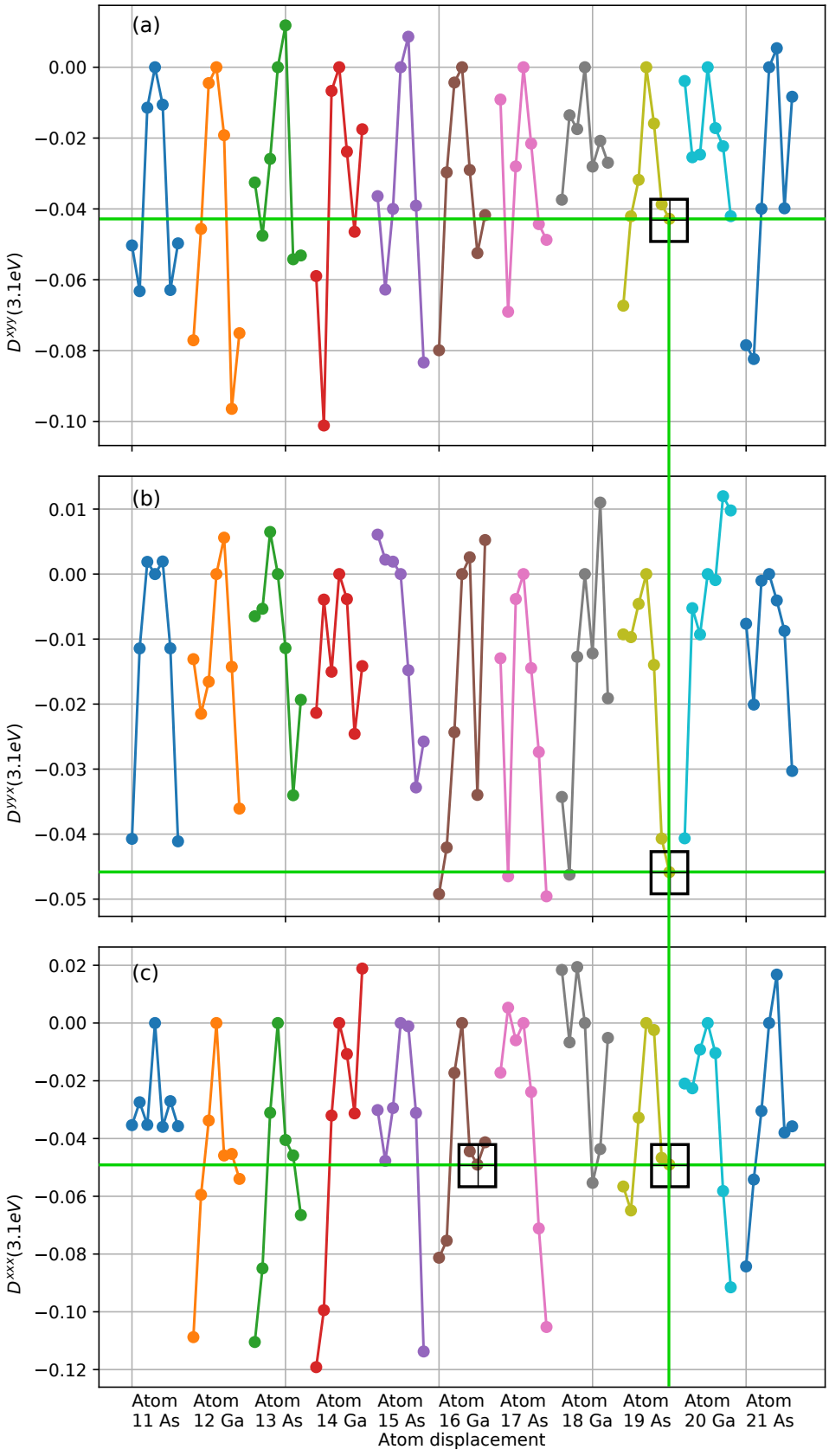

Figure 4.9: Measurement example for a displacement in the 19-th (green horizontal line) atom. Coincidences are marked as black boxes.

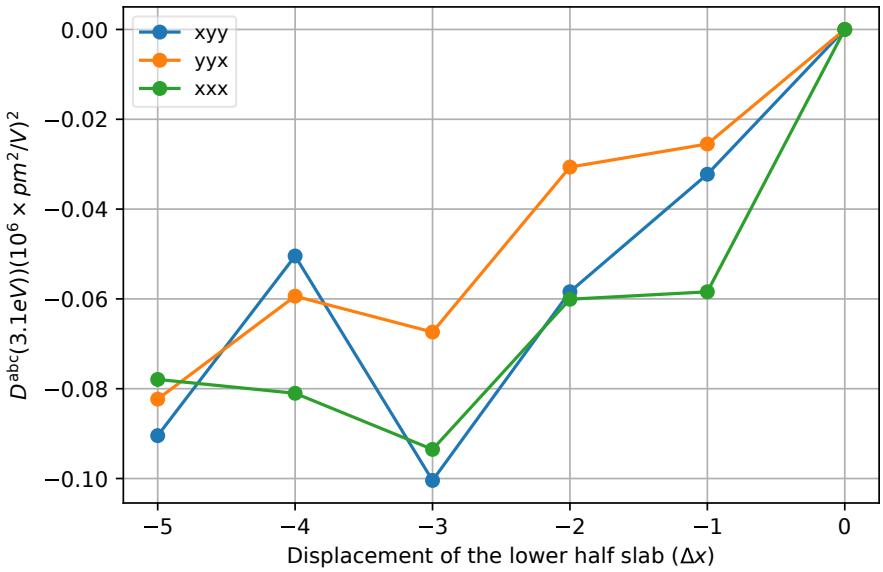

Figure 4.10: Difference of the nonlinear susceptibility of the displaced lower half with the relaxed case. For the calculated displacements the three lines did not crossed at the same point.

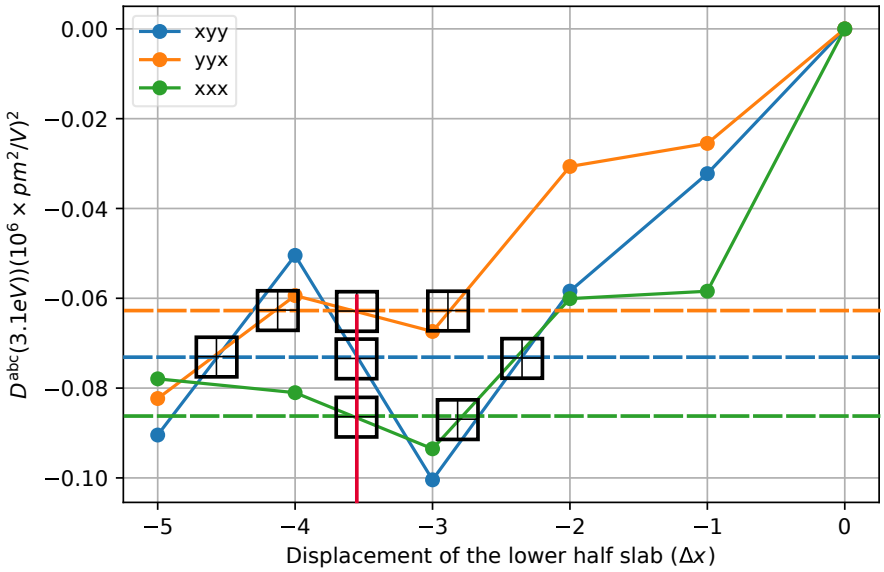

Figure 4.11: Measurement example for an induced misfit, the doted lines represent the simulated experimental measurement, the black squares represent the possible coincidences and finally the red line marks the only coincidence for the three tensor components and the value of the possible displacement.

5 Final Remarks

We have presented the results of the GaAs(110) surface as a test model to prove the viability of the SHG as an optical probe of the morphology of buried surfaces. As a result of the calculations and the analysis, has been shown that SHG can be used to directly measure the defect caused by the displacement of one of the atoms of the periodic cell. For the case of displacements of the atoms in the central layer, the symmetric behaviour of the SHG signal makes dificult to meassure the position, then, the information about the layered response may be necessary to measure its displacement. SHG can also be used to measure the displacement of the staked slabs of noncentrosymmetric material. The characterization of this defects shows greater potential as they are directly applicable to measurement of the dislocation in buried films with slabs under strain as in [2].

Furthermore, this work can lay ground for more research: the resolution of the method can be explored, also we expect that in some time experimentalist will be able to obtain the optical contribution of selected parts of the crystal, as is done here with the cut function for layers.

In conclusion, during the development of this project we achieved the following goals:

- We developed scripts to schematically induce cristalline defects to a given material simulating a buried surface defects. This scripts can be run in parallel for the calculation of the SHG response and for processing output of TINIBA.

- The nonlinear susceptibility for the SHG of GaAs (110) surfaces was calculated using the cut function formalism and the contribution of nonlinear operators.

- The SHG can be used to directly measure periodic defects on crystalline slabs and mismatches between stacked slabs.

- The SHG capability to measure this defects depends of the value of $\sigma^{\mathrm{abc}}(2\omega)$ for the SHG frequency. Nevertheless it can be used even in low sensitivity zones for the GaAs(110), like in the 3.1 eV SHG emission for the Ti:sapphire SHG incident field.

- In order to use the method proposed in chapter 4, the three components of the tensor need to be measured. The selection of the components will depend of the material, because the ones with the most intense response will change due to the crystal structure of the material.

- This method strongly depends on the cut function to isolate the contribution to the optical response of sections of the buried surfaces of the material.

- This method can be expanded experimentally for ferroelectric materials. Even though calculations for ferroelectrics can not be done currently, a scheme for comparison, like the one in the figure 4.7 can be constructed through the ordered fabrication and measurement of this kind of organized defects.

Bibliography

[1] N Setter, D Damjanovic, L Eng, G Fox, Spartak Gevorgian, S Hong, A Kingon, H Kohlstedt, NY Park, GB Stephenson, et al. Ferroelectric thin films: Review of materials, properties, and applications. *Journal of applied physics*, 100(5):051606, 2006.

[2] Natalie D Foster, Bryce I Edmondson, John G Ekerdt, David J Smith, and Michael C Downer. Strain-dependence of χ (2) in thin film barium strontium titanate. *AIP Advances*, 9(2):025312, 2019.

[3] AA Tamburello-Luca, Ph Hebert, R Antoine, PF Brevet, and HH Girault. Optical surface second harmonic generation study of the two acid/base equilibria of eosin b at the air/water interface. *Langmuir*, 13(16):4428–4434, 1997.

[4] A Piron, PF Brevet, and HH Girault. Surface second harmonic generation monitoring of the anion methyl orange during ion transfer reactions across a polarised water 1, 2-dichloroethane interface. *Journal of Electroanalytical Chemistry*, 483(1-2):29–36, 2000.

[5] Baptiste Blanc, Oriane Bonhomme, Pierre-Francois Brevet, Emmanuel Benichou, Christophe Ybert, and Anne-Laure Biance. Electroosmosis near surfactant laden liquid–air interfaces. *Soft matter*, 14(14):2604–2609, 2018.

[6] John F McGilp, Mark Cavanagh, John R Power, and J Des O'Mahony. Probing semiconductor interfaces using nonlinear optical spectroscopy. *Optical Engineering*, 33(12):3895–3901, 1994.

[7] SV Govorkov, VI EmelâĂŹYanov, NI Koroteev, GI Petrov, IL Shumay, and VV Yakovlev. Inhomogeneous deformation of silicon surface layers probed by second-harmonic generation in reflection. *JOSA B*, 6(6):1117–1124, 1989.

[8] Robert M Corn and Daniel A Higgins. Optical second harmonic generation as a probe of surface chemistry. *Chemical reviews*, 94(1):107–125, 1994.

[9] Renlong Zhou, Xiaoshuang Chen, Yingyi Xiao, Bingju Zhou, Lingxi Wu, Xiaojuan Liu, Yongyi Gao, and Jie Zhan. Second-order nonlinearity in triangular lattice perforated gold film due to surface plasmas resonance. *The Scientific World Journal*, 2014, 2014.

[10] Prashanth Panta, Chih-Wei Lu, Piyush Kumar, Tuan-Shu Ho, Sheng-Lung Huang, Pawan Kumar, C Murali Krishna, K Divakar Rao, and Renu John. Optical coherence tomography:

Emerging in vivo optical biopsy technique for oral cancers. In *Oral Cancer Detection*, pages 217–237. Springer, 2019.

[11] K König, HG Breunig, R Bückle, M Kellner-Höfer, M Weinigel, E Büttner, W Sterry, and J Lademann. Optical skin biopsies by clinical cars and multiphoton fluorescence/shg tomography. *Laser Physics Letters*, 8(6):465, 2011.

[12] Robert R Alfano, Yici Guo, Feng Liu, and Ping Pei Ho. Non-linear optical tomography of turbid media, March 27 2001. US Patent 6,208,886.

[13] Robert W Boyd. *Nonlinear optics*. Elsevier, 2003.

[14] JE Sipe and Ed Ghahramani. Nonlinear optical response of semiconductors in the independent-particle approximation. *Physical Review B*, 48(16):11705, 1993.

[15] Zachary H Levine. Optical second-harmonic susceptibilities: Frequency-dependent formulation with results for gap and gaas. *Physical Review B*, 49(7):4532, 1994.

[16] Claudio Aversa and JE Sipe. Nonlinear optical susceptibilities of semiconductors: Results with a length-gauge analysis. *Physical Review B*, 52(20):14636, 1995.

[17] Sergey N Rashkeev, Walter RL Lambrecht, and Benjamin Segall. Efficient ab initio method for the calculation of frequency-dependent second-order optical response in semiconductors. *Physical Review B*, 57(7):3905, 1998.

[18] Zachary H Levine and Douglas C Allan. Calculation of the nonlinear susceptibility for optical second-harmonic generation in iii-v semiconductors. *Physical review letters*, 66(1):41, 1991.

[19] Sergey V Faleev, Mark Van Schilfgaarde, and Takao Kotani. All-electron self-consistent g w approximation: Application to si, mno, and nio. *Physical review letters*, 93(12):126406, 2004.

[20] M Shishkin and G Kresse. Self-consistent g w calculations for semiconductors and insulators. *Physical Review B*, 75(23):235102, 2007.

[21] Pierre Hohenberg and Walter Kohn. Inhomogeneous electron gas. *Physical review*, 136(3B):B864, 1964.

[22] Leonard Kleinman and DM Bylander. Efficacious form for model pseudopotentials. *Physical Review Letters*, 48(20):1425, 1982.

[23] Norman Troullier and José Luís Martins. Efficient pseudopotentials for plane-wave calculations. *Physical review B*, 43(3):1993, 1991.

[24] F Nastos, B Olejnik, Karlheinz Schwarz, and J E. Sipe. semiconductors. *Physical Review B*, 72(4):045223, 2005.

[25] JL Cabellos, Bernardo S Mendoza, MA Escobar, F Nastos, and JE Sipe. Effects of nonlocality on second-harmonic generation in bulk semiconductors. *Physical Review B*, 80(15):155205, 2009.

[26] N Arzate and Bernardo S Mendoza. Microscopic study of surface second-harmonic generation from a clean si (100) c (4× 2) surface. *Physical Review B*, 63(12):125303, 2001.

[27] JE Mejía, C Salazarb, and Bernardo S Mendoza. Layer-by-layer analysis of second harmonic generation at a simple surface. *Revista mexicana de física*, 50(2):134–139, 2004.

[28] Lucia Reining, R Del Sole, M Cini, and Jiang Guo Ping. Microscopic calculation of second-harmonic generation at semiconductor surfaces: As/si (111) as a test case. *Physical Review B*, 50(12):8411, 1994.

[29] Bernardo S Mendoza and W Luis Mochán. Second harmonic surface response of a composite. *Optical Materials*, 29(1):1–5, 2006.

[30] Nicolas Tancogne-Dejean, Bernardo S Mendoza, and Valérie Véniard. Effect of material properties on the accuracy of antiresonant approximation: Linear and second-order optical responses. *Physical Review B*, 90(3):035212, 2014.

[31] Sean M Anderson, Nicolas Tancogne-Dejean, Bernardo S Mendoza, and Valérie Véniard. Theory of surface second-harmonic generation for semiconductors including effects of nonlocal operators. *Physical Review B*, 91(7):075302, 2015.

[32] Yujin Cho, Farbod Shafiei, BS Mendoza, Ming Lei, Tengfei Jiang, PS Ho, and MC Downer. Second-harmonic microscopy of strain fields around through-silicon-vias. *Applied Physics Letters*, 108(15):151602, 2016.

[33] Sean M. Anderson, Nicolas Tancogne-Dejean, Bernardo S. Mendoza, and Valérie Véniard. Improved ab initio calculation of surface second-harmonic generation from si(111)(1 × 1):h. *Phys. Rev. B*, 93:235304, Jun 2016.

[34] Sean M. Anderson and Bernardo S. Mendoza. Three-layer model for the surface second-harmonic generation yield including multiple reflections. *Phys. Rev. B*, 94:115314, Sep 2016.

[35] Sean M. Anderson and Bernardo S. Mendoza. Depth-dependent three-layer model for the surface second-harmonic generation yield. *Frontiers in Materials*, 4:12, 2017.

[36] Sean M Anderson, Yujin Cho, and Bernardo S Mendoza. General theory for the surface second-harmonic generation yield. *arXiv preprint arXiv:1712.04991*, 2017.

[37] Bernardo S Mendoza, F Nastos, N Arzate, and JE Sipe. Layer-by-layer analysis of the linear optical response of clean and hydrogenated si (100) surfaces. *Physical Review B*, 74(7):075318, 2006.

[38] L. Reining, R. Del Sole, M. Cini, and J. G. Ping. Microscopic calculation of second-harmonic generation at semiconductor surfaces: As/si(111) as a test case. *Physical Review B*, 50(12):8411–8422, 1994.

[39] In Ref. 49, a non hermitian operator was used in the context of linear optical response.

[40] N. Tancogne-Dejean, B. S. Mendoza, and V. Véniard. Effect of material properties on the accuracy of antiresonant approximation: Linear and second-order optical responses. *Physical Review B*, 90(3):035212, July 2014.

[41] Bernardo Mendoza Santoyo, José Luis Cabellos Quiroz, and Tonatiuh Rangel Gordillo. Tiniba: Programas para el cálculo en paralelo de respuestas ópticas en semiconductores usando un cluster de computo. Registrado ante el Instituto Nacional de Derechos de Autor (INDAUTOR-México) con número de registro 03-2009-120114033400-01.

[42] The ABINIT code is a common project of the Universitè Catholique de Louvain, Corning Incorporated, and other contributors (URL http://www.abinit.org). X. Gonze, et al. Computational Materials Science, 25, 478 (2002); X. Gonze, et al., Zeit. Crystallogr, 220, 558 (2005).

[43] N. Troullier and J. L. Martins. Efficient pseudopotentials for plane-wave calculations. *Physical Review B*, 43(3):1993–2006, January 1991.

[44] L. Kleinman and D. M. Bylander. Efficacious form for model pseudopotentials. *Physical Review Letters*, 48(20):1425–1428, 1982.

[45] For bulk calculations schemes of the SH susceptibility tensor beyond the independent particle approximation see for instance Refs. 50–57.

[46] A Huijser, J Van Laar, and TL Van Rooy. Angle-resolved photoemission from gaas (110) surface states. *Physics Letters A*, 65(4):337–339, 1978.

[47] Iván Prieto González. Design, fabrication and characterization of photonic crystals for cavity quantum electrodynamics enhanced devices. 2014.

[48] R Dorn, H Lüth, and GJ Russell. Adsorption of oxygen on clean cleaved (110) gallium-arsenide surfaces. *Physical Review B*, 10(12):5049, 1974.

[49] C. Hogan, R. Del Sole, and G. Onida. Optical properties of real surfaces from microscopic calculations of the dielectric function of finite atomic slabs. *Physical Review B*, 68(3):035405, 2003.

[50] B. Adolph and F. Bechstedt. Influence of crystal structure and quasiparticle effects on second-harmonic generation: Silicon carbide polytypes. *Physical Review B*, 62:1706, 2000.

[51] R. Leitsmann, W. Schmidt, P. Hahn, and F. Bechstedt. Second-harmonic polarizability including electron-hole attraction from band-structure theory. *Physical Review B*, 71(19):195209, 2005.

[52] E. Luppi, H. Hübener, and V. Véniard. Ab initio second-order nonlinear optics in solids: Second-harmonic generation spectroscopy from time-dependent density-functional theory. *Physical Review B*, 82:235201, 2010.

[53] E. Luppi, H. Hübener, and V. Véniard. Communications: Ab initio second-order nonlinear optics in solids. *The Journal of Chemical Physics*, 132(24):241104, 2010.

[54] H. Hübener, E. Luppi, and V. Véniard. Ab initio calculation of many-body effects on the second-harmonic generation spectra of hexagonal sic polytypes. *Physical Review B*, 83:115205, 2011.

[55] M. L. Trolle, G. Seifert, and T. G. Pedersen. Theory of excitonic second-harmonic generation in monolayer MoS2. *Physical Review B*, 89(23):235410, June 2014.

[56] C. Attaccalite and M. Grüning. Nonlinear optics from an ab initio approach by means of the dynamical berry phase: Application to second- and third-harmonic generation in semiconductors. *Phys. Rev. B*, 88:235113, 2013.

[57] M. Grüning and C. Attaccalite. Second harmonic generation in h-bn and mos_2 monolayers: Role of electron-hole interaction. *Phys. Rev. B*, 89:081102, 2014.